FEM simulation of the linear friction welding of titanium alloys

J. Sorina-Müller [a],[*], M. Rettenmayr [a], D. Schneefeld [b], O. Roder [b], W. Fried [a]

[a] FSU Jena, Löbdergraben 23, 07743 Jena, Germany
[b] MTU Aero Engines, Dachauer Straße 665, 80995 Munich, Germany

ARTICLE INFO

ABSTRACT

The complete process of linear friction welding of Ti6Al2Sn4Cr6Mo in two conditions (β- and α + β-forged) was simulated using the Finite Element Method. A full structural–thermal coupled transient 3D-analysis was conducted. Two different industry-relevant geometries of contact area (prismatic and blade like) were chosen. The axial shortening–time dependences were calculated. The results are analysed and compared with experimental data including microstructure and hardness profiles.

© 2010 Elsevier B.V. All rights reserved.

1. Introduction

Friction welding (FRW) is a solid state welding process [1] in which the heat for welding is produced by the relative motion of the two pieces being joined. Two principal FRW methods, direct-drive welding and inertia-drive welding, are applied for joining parts with rotational symmetry. For other geometries radial, orbital and linear reciprocating motions, respectively, are used. The present study focuses on linear friction welding (LFW) which is increasingly applied in numerous industrial branches such as automobile, aircraft, spacecraft building, manufacture of tools, electrical industry, and pipeline construction. LFW can also be used to join large polymer parts such as car bumpers, trunk lids and floor pans, and to make multiple welds in plastics or metals [2]. One successful application of LFW is the welding of aircraft engine blades to disks (BLISK = integrally BLaded dISKs). With LFW dissimilar materials can be joined, thus allowing to use the optimum alloys for the blade (exposed to high cycle fatigue and high temperature) and disk (exposed to low cycle fatigue).

LFW is used to join non-axisymmetrical components at their flat faces. Friction is generated through relative reciprocating motion between two workpieces. One of the pieces is held stationary, the other one oscillates linearly under compressive forces without the need for external heat and an additional welding substance. Once sufficient heat has been generated, the relative movement is stopped and a forging force is applied.

According to Vairis and Frost [3], LFW occurs in four distinct phases, particularly the initial phase, the transition phase, the equilibrium phase and the deceleration (or forging) phase. A detailed description of these phases can be found in [3,4]. Additionally to the four phases mentioned by Vairis, a fifth phase – the stand phase – can be introduced. According to the calculations the temperatures in the contact zones after the complete stop of the oscillation are still about 800–950 K. Recrystallization and creep can still proceed. During cooling, the material in the heat-affected zone shrinks. The forging pressure is held for a sufficiently long time (5–9 s) to consolidate the weld joint. The inert gas is then cut off and pressure reduced. Both parts remain clamped until they have cooled down to room temperature.

The friction between the faying areas, the efficiency of the welding, the plastic deformation during the upsetting and the strength of the joints are strongly temperature-dependent. Hence, over the years a substantial body of research has been established that applies mathematical and experimental methods to define the temperature fields within the welded parts. However, the measurement of the temperature distribution is only possible with a considerable degree of uncertainty. With the development of computer technology and numerical analysis, Finite Element simulation has become a powerful and reliable technique for the prediction of temperature and stress fields within the welded parts.

Generally simulations of temperature distributions are based on severe simplifications and thus only provide approximations for the real temperatures. Examples for simplifying assumptions are that the process-related upsetting is neglected [5,6], the material's

* Corresponding author.
E-mail address: P2soju@uni-jena.de (J. Sorina-Müller).

properties are assumed to be temperature independent [7–10], and the temperature profile is considered only in axial direction [5,7–10], although the radial temperature gradient for short friction times and large cross-sections is often steep [11]. In some cases the frictional heat is measured or calculated separately and then applied to the modeled friction surfaces [12–14]. Additionally, the heat loss due to radiation and convection is generally neglected [5,7,12,14,15]. A further example is that a linear rate of shortening and an equal amount of upset for both the stationary and the moving piece are assumed [6,12]. Overall it can be stated that the computation of transient temperature distributions in the welds of dissimilar materials is very challenging because of the diverse continuously changing material's properties in the heated zone of each piece. As a consequence, only a few research groups got involved with this research [11,16–19].

Available literature on friction welding, the basic data provided by welding machine manufacturers, and scientific investigations generally refer to the joining of equal cross-sections with simplified geometries such as cylindrical or prismatic contact areas. However, D'Alvise et al. [19] presented a 2D-simulation of inertia friction welding of workpieces made of dissimilar materials and with different cross-sectional dimensions. A powerful contact algorithm and automatic remeshing were implemented to model the flash formation at the interface, and realistic results were achieved. Also, Sluzalec [20] has developed a two-dimensional, thermal elastic–plastic FEM model for rotational friction welding (RFW) and has obtained a satisfactory agreement between computed and measured temperatures.

As RFW and LFW differ substantially in the heat distribution in the rubbing interface, the documented information about processing parameters and physical processes of RFW cannot be directly applied to LFW. The few available numerical simulations of LFW and their analysis refer to the modeling of the LFW process until the beginning of axial shortening [21]. However, the computation of the upsetting during LFW has, to the best knowledge of the authors, not yet been published.

The simulation of friction welding presented here aims to model the process of linear friction welding and to analyse typical industry-relevant parameter and geometries using realistic boundary conditions. The described work investigates the temperature field as a function of the various processing parameters at any point in time during the welding process and computes the axial shortening vs. time for the joining the similar or dissimilar materials.

2. FE – modeling strategy

The Finite Element Method (FEM) allows for the consideration of both the temperature dependent material's properties and non-linear boundary conditions. The software package ANSYS was used for the simulation of the thermal and structural fields.

The main friction welding parameters and the material's properties required for the analysis are summarised in Table 1.

The range of process parameters taken from the welding protocols and used in the simulation are given in Table 2.

2.1. Geometry

Samples with two different cross-section geometries, particularly prismatic and simplified blade like (Fig. 1a and b), were chosen for the analysis. Both samples were of the same chuck dimensions. The nominal cross-section area of the prism is almost twice that of the specimen with the blade like geometry. Z-direction was defined such that negative values of z correspond to the stationary part and positive values of z to the moving part. The oscillatory movement along the shortest side (Y-axis) of the piece was chosen. This provides a better possibility for the plasticised layer to be expelled into the flash and leads to welded joints with better quality.

Details of the processing conditions as well as geometry of the blade like piece are not given in this paper due to their proprietary nature. The duration of the process was controlled by axial shortening.

Table 2
Process parameter.

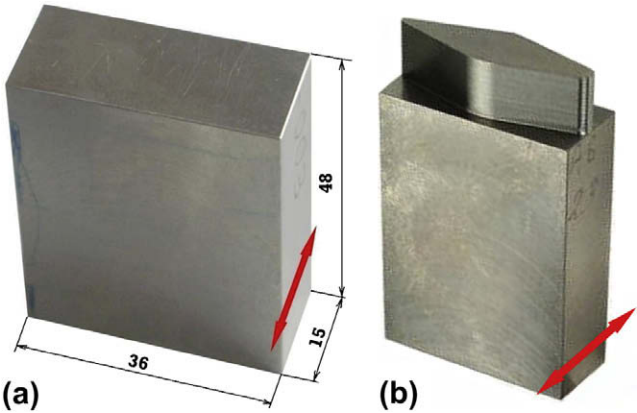| Frequency (Hz)	Amplitude (mm)	Axial force (kN)
20–35	1.5–2.2	3–55

Fig. 1. Samples with prismatic (a) and blade like (b) geometry. The arrows indicate the direction of friction motion.

Table 1
Input and output parameters during the simulation.

Input parameters	Process parameter:	Material properties:
	– Frequency (f)	– Density $\rho(T)$
	– Amplitude of oscillation (u_0)	– Young's modulus $E(T)$
	– Axial force ($N(t)$) or pressure ($p(t)$), where t is the process time	– Poisson's number $v(T)$
	– Axial shortening (s)[(1)]	– Coefficient of thermal expansion $\alpha(T)$
	or	– Enthalpy $H(T)$
	– Complete process time (t_c)[(2)]	– Thermal conductivity $\lambda(T)$
		– Thermal contact conductance coefficient $h(P)$
		– Friction coefficient $\mu(T)$
		Inert gas properties:
		– Convection coefficient α^C
		– Ambient temperature T_∞
Output arameters	– [(1)]The complete process time or [(2)] the complete axial shortening	
	– Axial shortening $s(t)$ as a function of process time	
	– Time-dependent temperature distribution $T(x, y, z, t)$	

2.2. Meshing

As the temperature field is highly transient and material's properties are strongly temperature dependent, the mesh density and the time increment were chosen according to the steepest temperature gradients. For modeling of the heat transfer generated by friction, a 3D hexahedron element *Solid226* [22] with quadratic shape function was chosen. Because the heat-affected zone (HAZ) is small, only a part of the samples near the rubbing interface (for prismatic samples $36 \times 15 \times 30$ mm^3) was selected for computing and meshed (Fig. 2).

The contact area between the two sliding surfaces was modeled with 3D, 8-node, higher order quadrilateral elements *Conta174* and *Targe170* (both deformable bodies). Along the steepest temperature gradients (direction of upsetting) in the HAZ, the finest elements were generated with a side length of 0.125 mm.

2.3. Constraints and loads definition

The bottom part (stationary) was constrained in all directions along its bottom face (Γ_3, Fig. 3). The exterior faces (Γ_4) of the stationary piece were fixed along the X- and Y-axis. The exterior faces of the moving piece (Γ_5) are fixed along the X-axis and assigned a reciprocating displacement along Y. The displacement changes with time t according to a sinusoidal function with the required frequency f of oscillation and amplitude u_0

$$u = u_0 \cdot \sin(2\pi \cdot f \cdot t) \qquad (1)$$

As long as the surfaces are in sliding contact ($\Gamma_{contact}$), the friction law of Coulomb is applied and frictional work is generated. To define the mechanical behaviour of the surfaces, a number of associated data are necessary, particularly the friction coefficient taken from the experiments and the parameters for the numerical simulation of the deformable bodies.

The pressure is applied on the top surface (Γ_2) of the moving piece.

As initial thermal condition, a uniform temperature of 293 K is applied to both samples. The temperatures of the environment and of the chuck system are also set to 293 K.

It is shown experimentally in [23] that during friction of metallic materials most frictional energy is spent on heating. According to [6], the fraction of frictionally dissipated energy converted into heat *fhtg* is about 90%. This value is also used here.
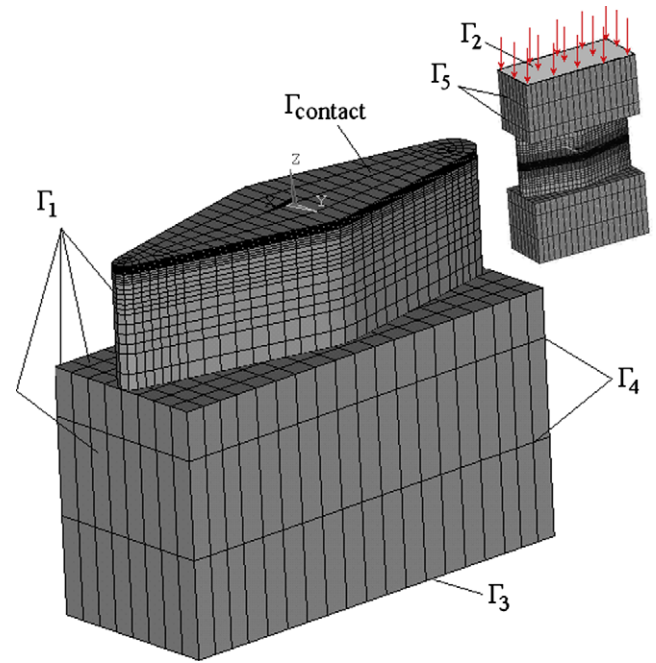

Fig. 3. Constraints and load areas.

The weight factor for the distribution of heat *hdf* between two contact surfaces is calculated according to [16] for dissimilar materials as

$$hdf = \frac{q_2}{q_1} = \sqrt{\frac{\lambda_1 \cdot \rho_1 \cdot c_{p1}}{\lambda_2 \cdot \rho_2 \cdot c_{p2}}} \qquad (2)$$

where λ is thermal conductivity, ρ the density and c_p the specific heat. The indices 1 and 2 denote the materials of the parts to be welded. The total heat is the sum of both factors $q = q_1 + q_2$. For identical materials, the heat is distributed equally.

The rate of frictional dissipation is given by

$$q = fhtg \cdot \tau \cdot v \qquad (3)$$

where T is the equivalent frictional stress, V is the sliding rate.

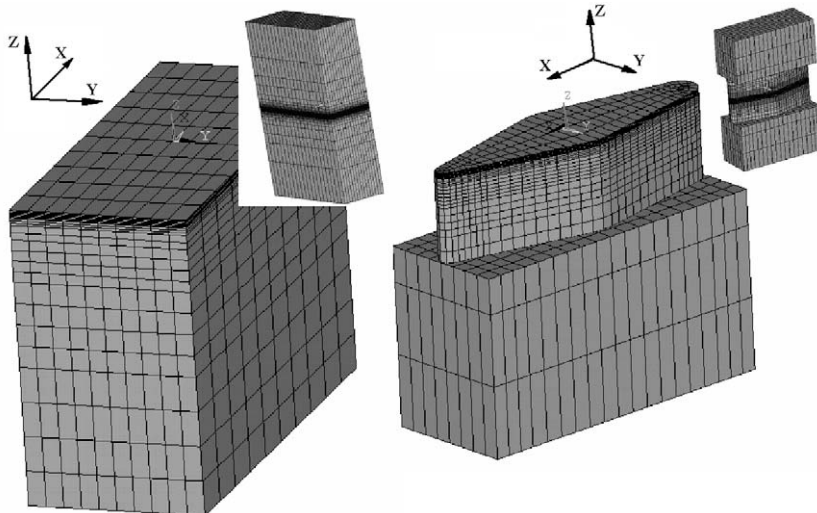The amount of frictional dissipation on contact surfaces is defined by

Fig. 2. Meshing of the prismatic and blade like parts; small pictures show the assemblies of the prismatic and blade like parts prior to the friction.

$$q_1 = \frac{1}{1+hdf} \cdot fhtg \cdot \tau \cdot v \qquad (4)$$

and

$$q_2 = \frac{hdf}{1+hdf} \cdot fhtg \cdot \tau \cdot v \qquad (5)$$

The thermal contact conductance h during the initial phase consists of conduction through the series of actual contact spots between the two contacting areas. The radiation in the interfacial gap due to the surface roughness is neglected, because the temperatures at the joint were not in excess of 573 K [24]. The interfacial gap thickness is too small for a convection current to be set up and is also neglected, which is even more justified due to the short duration of the initial phase. According to [24] the solid spot heat conduction is determined as a function of the surface parameters, material's properties and contact pressure for the friction pairs Ti64, Ti6246 β/β and Ti6246 $\beta/\alpha + \beta$.

According to [25] the conductive heat transfer between two contacting surfaces is defined as

$$q_c = h(T_1, T_2, p) \cdot (T_1 - T_2) \qquad (6)$$

where T_1, T_2 are the temperatures of the contact points on the faying surfaces and p is the contact pressure.

In order to model the convective heat transfer for the external surfaces (Γ_1), a heat convection coefficient of 100 W/(m^2 K) was chosen. This is a justified assumption for forced flow situations, similar to those encountered in the surroundings of the two moving specimens [3]. If nodes of the faying surfaces move out from the contact, the heat convection between the contact surfaces ($\Gamma_{contact}$) and the environment is taken into account.

2.4. FEM formulation

The process was separated into a mechanical and a thermal problem to be solved in parallel during every time step of the analysis.

Thermal–structural coupling (weak or sequential) in the matrix equation is given in a general form [22]:

$$\begin{bmatrix} [M] & [0] \\ [0] & [0] \end{bmatrix} \cdot \begin{Bmatrix} \{\ddot{U}\} \\ \{\ddot{T}\} \end{Bmatrix} + \begin{bmatrix} [C] & [0] \\ [0] & [C^T] \end{bmatrix} \cdot \begin{Bmatrix} \{\dot{U}\} \\ \{\dot{T}\} \end{Bmatrix}$$
$$+ \begin{bmatrix} [K] & [0] \\ [0] & [K^T] \end{bmatrix} \cdot \begin{Bmatrix} \{U\} \\ \{T\} \end{Bmatrix} = \begin{Bmatrix} \{F\} \\ \{Q\} \end{Bmatrix} \qquad (7)$$

where $[M]$ is the mass matrix; $[C]$ the damping matrix; $[C^t]$ the thermal specific heat matrix and $[K]$ the stiffness matrix. $[K^t] = [K^{tb}] + [K^{tc}]$ is the thermal conductivity matrix that consists of the thermal conductivity matrix of material $[K^{tb}]$ and the thermal conductivity matrix of convection surface $[K^{tc}]$; $\{F\} = \{F^{nd}\} + \{F^{th}\}$ is the load vector that consists of the applied nodal force vector $[F^{nd}]$ and the thermal strain force vector; $\{Q\} = \{Q^{nd}\} + \{Q^c\}$ is the heat flow vector that consists of the applied nodal heat flow rate vector $\{Q^{nd}\}$ and the convection surface vector $\{Q^c\}$; $\{T\}$ – temperature vector and $\{U\}$ - displacement vector, $\cdot$ – time derivative, $\cdot\cdot$ – second time derivative.

For solving the pre-conditioned Conjugate Gradient, an iterative equation solver (PCG-Solver) was used with non-symmetric matrices of elements as well as penalty-based methods for contact analysis [22]. To improve the convergence during the transient analysis, the time step increment t_i is defined as [26]:

$$t_i = \frac{\Delta^2}{4k} = \frac{\Delta^2 \rho \cdot C_p}{4\lambda} \qquad (8)$$

where Δ is the shortest length of the element along the highest temperature gradient, k is thermal diffusivity. The value $t_i = 2 \times 10^{-3}$ s is calculated for this analysis.
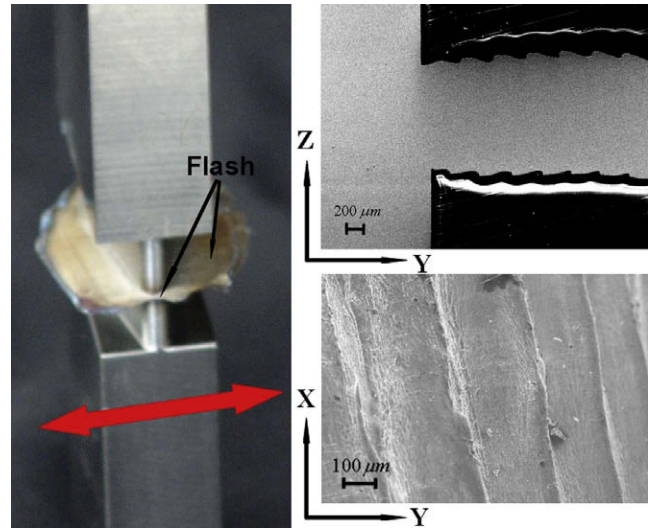

Fig. 4. Form of the flash after welding (left) and flash micrograph with a section (right top) and view on the flash (right bottom).

2.5. Modeling of axial shortening

During the friction process the material is heated, plastically deformed and finally expelled due to the applied friction pressure and oscillatory movement, i.e. the flash is occurring. It also comprises a series of ripples (Fig. 4 top right) due to the reciprocating motion. It is concluded that axial shortening proceeds stepwise. Additionally, the flash perpendicular to the direction of motion shows generally little evidence of ridges.

In analogy to the stepwise upsetting of material which was observed in this work and earlier work in the literature [3,21,27], a stepwise elimination of the deformed mesh has been developed to simulate the pulsing action of material flow.

After the material near the contact zone was heated, the new model without material to be eliminated was constructed and a new analysis was restarted. From the modeling results of the former step, the temperatures and displacements were saved and assigned to the remaining nodes of the new model. For the following computations, first the contact elements were newly established, and the structural and thermal boundary conditions as well as the loads were defined. The analysis was then continued.

In the analysis, a specifically developed module was implemented that allows a successive remeshing during the axial shortening. First, the mesh was fine only in close proximity to the contact area (Fig. 2). During the upsetting phase, the models were re-meshed, and the saved information was assigned to the remaining nodes. Information about the newly defined nodes was obtained through linear interpolation from the adjacent nodes. The employed approach minimises the number of nodes at the beginning of the analysis and thus reduces the necessary computation time.

3. Material and material's properties definition

The welds were performed on the heat-treatable, high-strength $\alpha + \beta$-titanium alloy Ti–6Al–2Sn–4Zr–6Mo (Ti6246) (chemical compositions in Table 3). In the β-forged state, this alloy offers an interesting alternative to Ti–6Al–4V (Ti64) and Ti–6Al–2Sn–4Zr–2Mo (Ti6242) for aero-engineering applications, since it has approximately 10–20% higher strength and toughness [28,29]. Ti6246 and Ti–5Al–2Sn–2Zr–4Mo–4Cr (Ti-17) are the only tested and certified high-strength ($\alpha + \beta$)-titanium alloys for rotating applications in aero-engines [30].

Table 3
Chemical composition of the materials. Note, that due to different thermo-mechanical treatment, microstructure and properties are substantially different (see Figs. 5–7).

Sn	Mo	Zr	Cu	Fe	Si	Al	C	O	N	H	Ti
1.98–2.0	6.01–6.09	3.99–4.05	<0.05	<0.07	0.04–0.05	5.93–5.99	⩽0.01	0.095–0.105	0.0015–0.0025	⩽0.003	Rest

Ti6246 samples were forged in two different ways to represent a typical disk (material A) and blade (material B) microstructure. The thermo-mechanical treatments applied to this alloy are presented in Table 4. They resulted in two different microstructures:

- A lamellar structure (material A) consisting of lamellar primary α_p in a β-forged matrix (Fig. 5a); this structure consists of a high volume fraction of secondary α_{sec} in the β-matrix between α_p-laths due to age hardening.
- A bimodal structure (material B) consisting of 28 ± 5 vol.% of globular primary α_p with an average grain size of 15 μm in a

Table 4
Thermo-mechanical treatments defined as solution treated and aged (STA acc. to [31]).

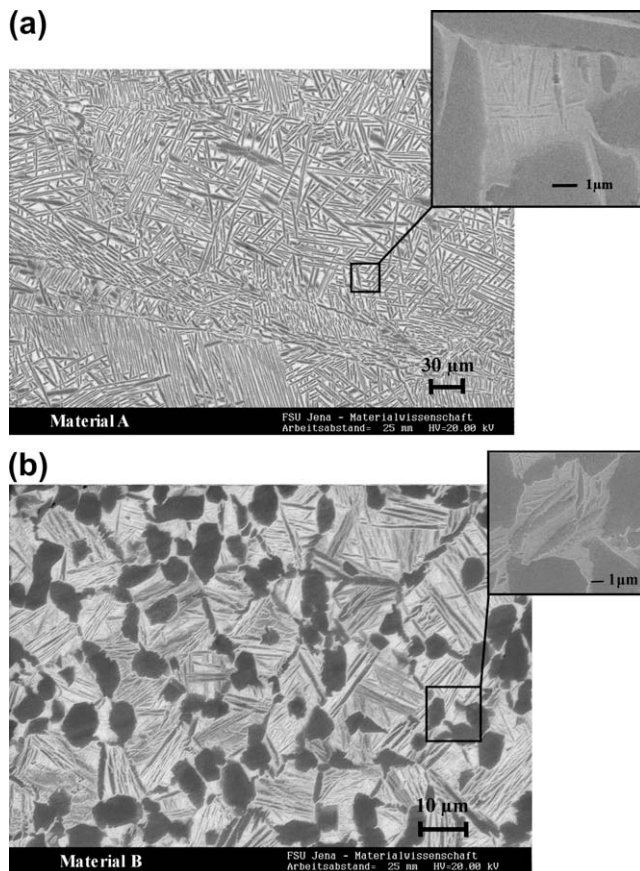|	Forging	Solution temperature, K, dwell time, h	Cooling from solution	Aging temperature, K, dwell time, h	Cooling from aging
Material A	β-Forging	1188/1 h	AC	868/8 h	AC
Material B	α + β-forging	1188/1 h	AC	868/8 h	AC

Fig. 5. REM micrograph of Ti6246 parent alloy, (a) material A, (b) material B. α phase appears dark grey while β phase appears bright.

lamellar (α + β)-matrix (Fig. 5b); this material has a lower toughness and a higher strength as compared to the β-forged Ti6246.

For the computation of temperature fields and residual stresses, the mechanical and thermal properties need to be known in the temperature range of 293–1593 K. In the specified temperature range, sufficient information was not available for the studied microstructures of Ti6246. Therefore it was necessary to establish the thermal and elastic material's properties through in-house measurements. An example for results of such measurements is shown in Fig. 6. The β-transformation range was derived from the linear thermal expansion and is approx. at 1208 K, which corresponds well to the results in [31]. In order to take the phase transformation into account, the enthalpy-function has been calculated for both states.

A friction coefficient μ(T, p) for the rubbing pairs material A – material A (AA) and material A – material B (AB) was determined using a combination of measurement [32] and simulation. During the experiment the temperatures at 3 mm distance from the actual rubbing interface were measured with thermocouples. To estimate the true temperatures at the interface, a non-linear finite element model with the same frequency, amplitude and axial force as applied in the experiment was used. By varying the model parameters, the simulated temperature field was adjusted to the measured temperatures. From the calculated temperatures in the rubbing interface and during the experiment recorded time-dependent friction forces, the friction coefficient was derived as a function of temperature in the applied pressure and velocity range. As shown in Fig. 7, the friction coefficient varies with temperature during the process, in agreement with experiments by Vairis and Frost [33] for Ti64. Furthermore, the studied friction pairs (AA, AB) show substantially different friction behaviour. The increase of the friction coefficient in the interval 400–600 K can be attributed to the stick–slip behaviour described in [34]. After the α + β → β phase transformation, the friction coefficient is assumed to be constant and equal for both Ti6246 conditions.

4. Results of modeling

4.1. Temperature distribution

All simulations were carried out with the same initial and boundary conditions. Typical temperature distributions are shown in Fig. 8.

The geometry of the contact interfaces has an effect on the temperature distribution in the weld and heat-affected zones (Fig. 8). In the present calculations, temperature differences at the contact interface of the specimens with blade like geometry up to 500 K (contact areas without edges within −14.8 mm < x < 15.8 mm, Fig. 8 left) were observed. At the edges which have a total area of less than 6% of the entire contact zone, the temperature differences (from the edges to the centre of the body) reached approx. 740–800 K. This is attributed to the very short time of overlap and to the losses via convection.

Apart from the temperature gradients in both of the contact areas and along the upsetting, the maximum temperature on the faying surfaces is also of great interest for the prediction of the resulting microstructure in the HAZ. The maximum temperatures
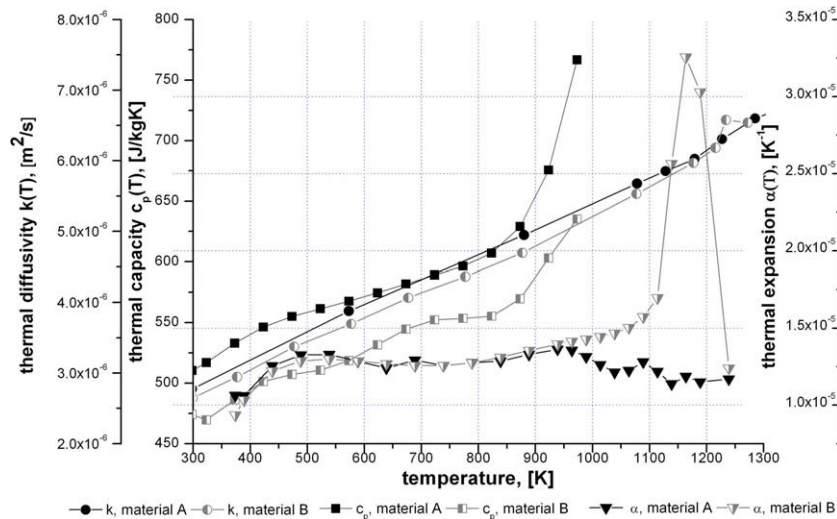
Fig. 6. Measured material's properties, thermal expansion was measured by dilatometry, heat capacity by differential scanning calorimetry and thermal diffusivity by laser flash method.
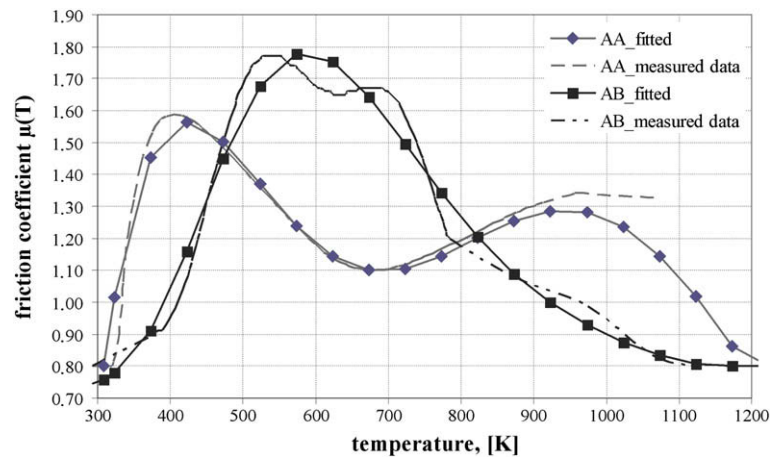

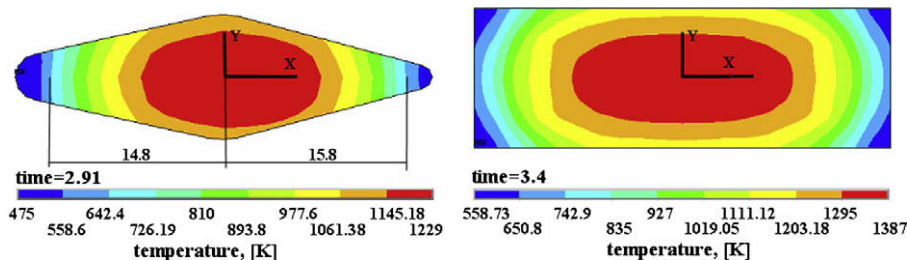**Fig. 7.** Friction coefficient as a function of temperature for friction pair Ti6246 β/β (AA), Ti6246 $\beta/\alpha + \beta$ (AB).

Fig. 8. Temperature distribution in the rubbing interface of the stationary part, material pair AA. The temperature is showed at the time when the desired upset is reached and the relative movement starts slowing down.

occur at the positions that are most difficult to measure. The calculated temperature evolution at some centre points is shown in Fig. 9. Under the chosen welding conditions and geometries, it can be concluded from the calculations that no liquid phase exists during the welding process. These results confirm experimental results by other researchers [3,27,35–39].

According to the computations, the temperature was increasing at the contact interface from 293 K to max. 1373 K before the onset of shortening. In the centre of the contact surface temperatures

above the $\alpha + \beta \rightarrow \beta$-transus were reached. This result was confirmed by metallography.

4.2. Axial shortening

The resulting axial shortening time dependences are shown in Fig. 10. The time until the onset of the upsetting is between 1.5 s and 2.5 s (in dependence on process parameter) and is in good agreement with the experiment. The comparison between experi-
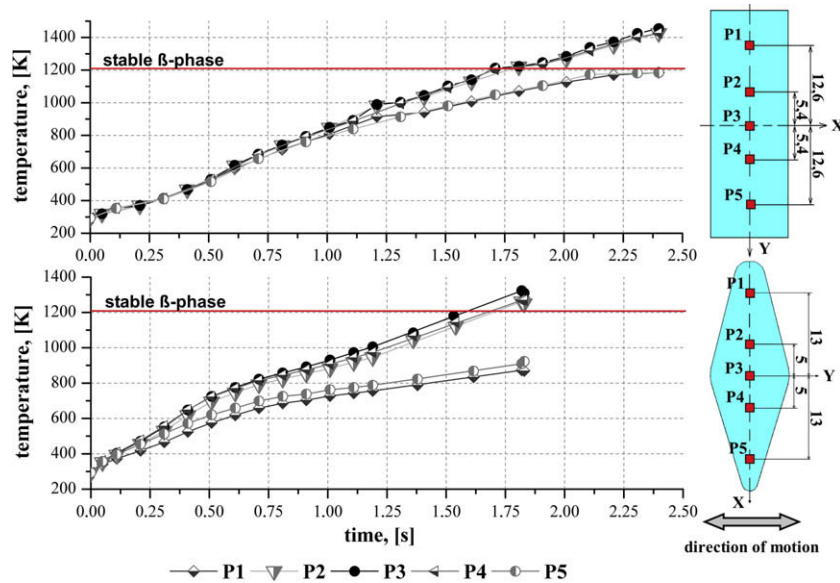
Fig. 9. The calculated temperature evolution in the rubbing interface of the stationary part at selected points before the onset of axial shortening, AA-weldings with prismatic and blade like geometries.
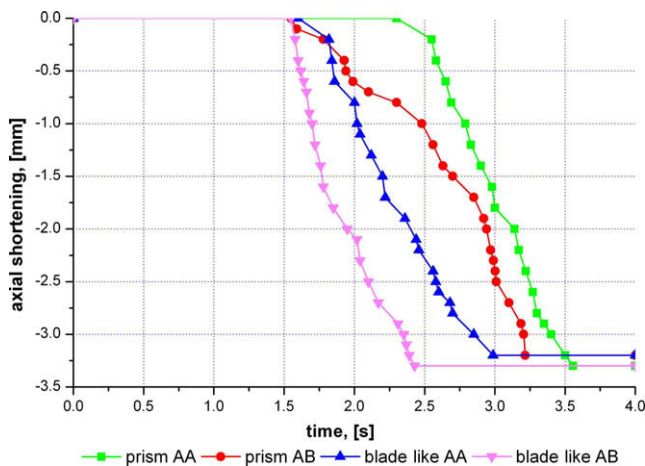

Fig. 10. Calculated axial shortening as a function of process time for prismatic and blade like geometries from friction pairs Ti6246 β/β (AA) and Ti6246 β/α + β (AB).

Fig. 11. Calculated mean temperature of the contact interface and pressure (standardized) as a function of processing time, samples with prismatic friction areas. Here, only the temperature of the lower part is shown owing to its high similarity to the lower one.

ment and simulation shows that the numerically calculated shortening starts earlier than the experimental one. The reason for this may be energy losses by radiation and by mechanical parts of the LFW machine. Both effects are neglected in the simulation.

4.3. Pressure dependence

As expected, the pressure plays a significant role for the heating of the contact surfaces. Due to the higher pressure, the prismatic rubbing pairs AB (Fig. 11) are heating faster (and higher) than the prismatic rubbing pairs AA. After 1 s, the pressure curves are almost identical, and the mean temperatures are increasing nearly parallel to each other. Here, differences in pressure during both analyses have a much greater influence on the temperature distribution than differences between the material's properties of A and B.

5. Validation of the results

For validating the results of the calculation, first the weld microstructure was analyzed and hardness profiles were mea-
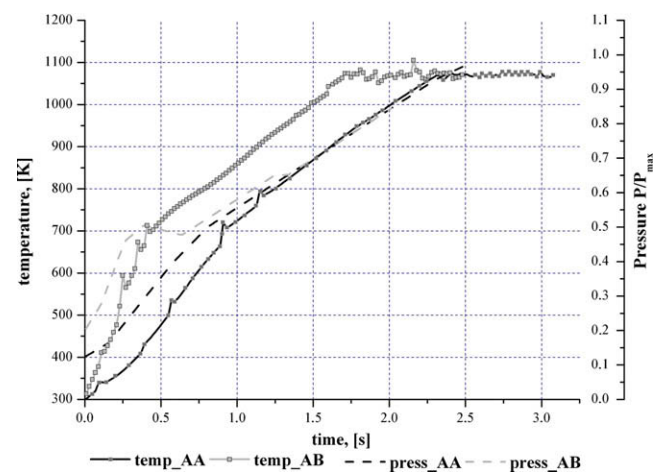
sured. The results of calculations were then compared with the experimental data from the present work and with data from the literature.

5.1. Microstructure analysis

Samples for optical microscopy were prepared by cutting welded joints in a central position, parallel to the direction of motion. The samples were mechanically ground, polished and slightly etched with Kroll's reagent (3 ml HF (40%ig) und 5 ml HNO_3 (65%ig) in 100 ml H_2O).

Examination of the weld interface in the linear friction bonded Ti6246 specimens revealed three distinct zones with a smooth transition in particularly the weld centre (WC) (I), the heat-affected zone HAZ (II) and the parent material (PM) (III), as shown in Fig. 12. No defects such as cracks and voids were observed in the weld joints.
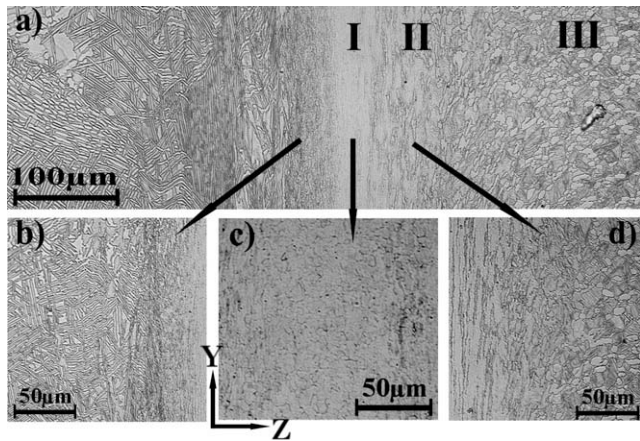
Fig. 12. Micrograph of a weld zone in a Ti6246 linear friction–welded sample: (a) a typical linear friction weld AB microstructure, (b and d) sudden onset of severe plastic deformation on both sides of the weld, (c) recrystallized grains in the weld line. W/o PWHT, OM. α phase appears bright grey while β phase appears dark.

5.1.1. WC (I)

The fine grained microstructure is a result of rapid heating during the welding to temperatures up to or above the α + β → β-transus temperature. This is characterized by severe plastic deformation, followed by fast cooling to room temperature. Due to its extremely fine granulation near the weld line, the microstructure cannot be resolved by SEM. Fine microstructures in the weld zone and the HAZ confirm that no liquid phase was produced during the process, as solidification microstructures are not expected to have a length scale below the resolution limit of the SEM.

Previous work on titanium alloys such as Ti–6Al–4V [27,40,41] and Ti–6.5Al–1.9Zr–3.3Mo–0.25Si [41] demonstrates that thermomechanical processing near or above the β-transus together with deformation and rapid cooling can produce dynamic recovery or recrystallisation, depending on the strain rate and strain conditions [27,35,42]. The recrystallisation temperature required is not a precisely definable material's parameter, but is dependent on the grain size and to some extent on the degree of deformation [43]. At high deformation degrees, recovery occurs by dislocation restructuring and formation and growth of sub-grains [44]. Fig. 12c indicates that restoration processes such as dynamic recrystallization are operative during linear friction welding. The occurrence of recrystallised grains (approx. ±10 μm) indicates that in spite of the short duration of the process (<1 s) this region exceeded the β-transus. In the single-phase beta region, recrystallization occurs more easily.

5.1.2. HAZ (II)

Further away from the weld line (starting from about 80 μm, Fig. 12b and d), the nature of the microstructure shows evidence of severe plastic deformation during the welding process on both sides of the weld. The original grains are heavily deformed and reoriented during the welding process in the direction of the friction motion and thus along the direction of material flow. Heavily deformed primary α grains can be generally found in the plastically affected zone. Sun et al. [37] found a high density of dislocations in the α-phase. However, in this region the temperatures achieved during the deformation process give rise to elongated retained β grains separating a large number of the α grains. The existence of fragmented grains of the bimodal microstructure suggests that the temperature at this location did not exceed the β-transus of 1208 K.

Further away from the weld, a completely undeformed region (III) follows. This region still belongs to the HAZ as there recovery and precipitate coarsening have occurred.

According to the computations, the material in the contact zone was heated to maximum 1373 K with an average rate of 900 K/s before the onset of shortening. Fu and Duan [13] have computed the rate of the temperature increase as 980 K/s during the RFW-process. There, the obtained peak temperature reached 1513 K. Furthermore, experiments conducted by Karadge et al. [40] have demonstrated that during LFW of prismatic Ti64-parts, temperatures above 1173 K could be reached directly at the contact interface. In similar experiments, Wanjara and Jahazi [27] have measured a peak temperature of 1373 K at the weld interface using a two-color pyrometer.

5.2. Temperature gradient

The different microstructures are reflected in the hardness, whose values first of all depend on the temperature gradient [36]. For the further characterization of the HAZ, the hardness profiles are shown in Fig. 13.
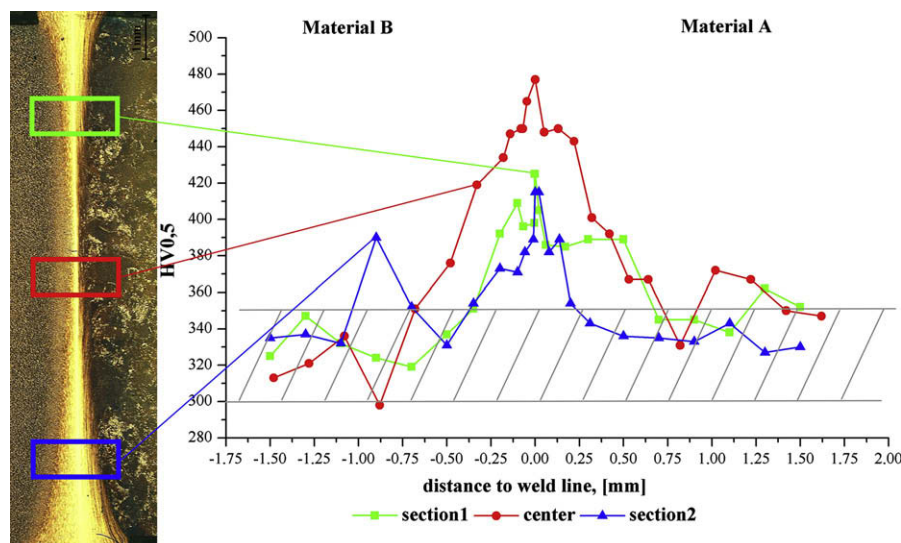

Fig. 13. Hardness profile measured parallel to the direction of the motion, welding AB with blade like geometry. The grey hatched zone represents the standard deviation of the hardness measured in the as-received material. The Sections 1 and 2 are at approx. 3.7 and 4.2 mm from the middle of oscillation.

From the hardness measurements it can be seen that the weld region is distinctly harder than the surrounding HAZ. The peak hardness (approx. 480 HV) was found in the weld centre. This increase in hardness relates to the parent material in the weld line region due to the grain refinement characteristics, which is influenced by the high temperatures.

Wanjara and Sun et al. [27,37] determined the hardness of Ti64 base material with bimodal structure as 349 HV and 330 HV respectively and for linear friction welded an average value of approximately 400 HV which confirms the hardness measurements in the present work.

According to [37], the highest hardness value appears in the phase-transformed region. Overall, based on the hardness measurements it is found that the highest hardness values (Fig. 13, centre) lie within 0.41 mm and 0.3 mm from the weld line for oscillating and stationary parts of the rubbing pair AA respectively and 0.3 mm and 0.2 mm for the rubbing pair AB. Numerical results show that the regions of phase transformation in the weld centre are of $z = \pm(0.35-0.4)$ mm which is in a good agreement with results from the hardness measurements. This finding together with the observation of the microstructure is consistent with previous work on linear friction welding of titanium alloys that indicates peak temperatures exceeding the β-transus at the weld interface [36,40,45].

Compared to the centre, other sections show lower hardness values. The decrease in hardness may be attributed to the fact that no $\alpha + \beta \rightarrow \beta$ phase transformation took place there. Furthermore the differences in the hardness profiles confirm the temperature gradients in the weld area which were computed here (Figs. 8 and 9). Kleiber and Fu [10,13] also reported significant differences in the radial temperature distribution during the RFW.

In Fig. 14, the different widths of the HAZ are shown for comparison of results of the computation and of the microstructure analysis as well as the hardness analysis of the welds. Both the FEM-calculations and analyses of microstructure and hardness show comparable widths of the HAZ. It is symmetric for the rubbing pair AA and asymmetric for the rubbing pair AB, where the HAZ in material B is wider.

5.3. Axial shortening

The accuracy of the computed axial shortening depends on the side length of the elements in the contact area. The mass expelled in the direction of the movement per half cycle of oscillation was found to be independent of the frequency for the studied range of amplitudes [3]. Due to the small side length of the elements in
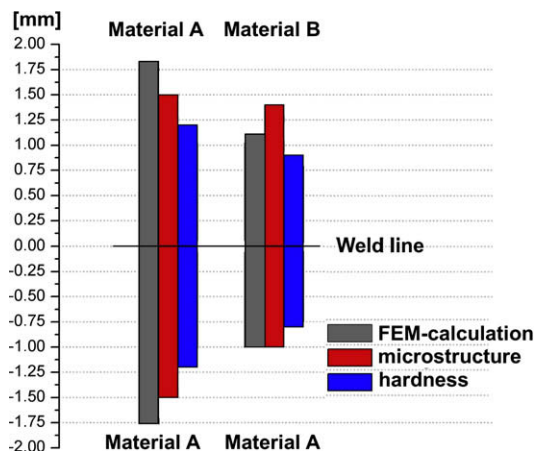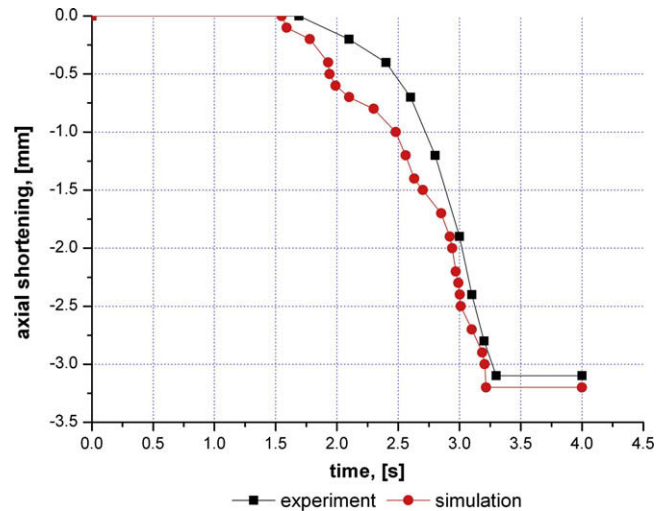

Fig. 15. Calculated and experimental axial shortening as a function of process time for prismatic welding from friction pair Ti6246 β/α + β (AB).

the direction of upsetting, the eliminated mass per half cycle is assumed to be independent on the process parameters. The heat loss through the expelled material is taken into account due to the fact that heated elements are removed from the contact area, while new and colder ones are coming into contact.

The computed axial shortening during the equilibrium phase generally deviates less then 10% (in some rare instances up to 20%) from the experiment. The final axial shortening generally deviates up to 5% (in some instances up to 10%), which is within the range of tolerance of the experimental welds. Such differences between the experimental and the simulation results occur due to slight variations in microstructure and hardness which are influenced by differences in the strain hardening during forging and heat treatment. An example of the calculated and experimental time dependences of the axial shortening for prismatic specimens is shown in Fig. 15.

The test computations with different measured temperature dependences of material's properties showed that even small fluctuations of material's properties can be responsible for comparably large deviations of the process flow.

The practicability of this simulation has been tested additionally by calculating the welding process of a real turbine blade–disk geometry made of Ti64. The resulting axial shortening deviates 5% from the experimental one.

6. Conclusions

The developed simulation

- calculates the temperature evolution at any point in time during the whole process of the linear welding until the complete stop of the oscillation;
- calculates the axial shortening as a function of process time for every part separately and for the both together;
- considers the friction flux as a result of movement between the two specimens, heat conduction from the rubbing interface to the bulk of the specimens, convection losses to the surrounding air as well as thermal contact conductance in the faying areas directly which could be achieved due to the three-dimensional modeling;
- considers the variation with time of the surface contact area, material's properties and the frictional parameters, with material's properties and friction coefficient changing with temperature.

Fig. 14. Comparison of width of the HAZ from the FEM calculation (here, HAZ is the zone with the temperature over 873 K), microstructure and hardness examinations.

For newly tested materials, geometries and processing parameters, reasonable agreement between experiments and numerical results concerning temperatures, axial shortening and the time necessary to obtain the desired amount of upset was achieved.

Some regions of the weld interface reach the temperature of $\alpha + \beta \rightarrow \beta$ phase transformation, which was confirmed through the microstructure analysis and supported by the hardness profile measurements. In the contact areas, the temperature differences up to 700 K can exist.

This simulation is a very useful qualitative predictive tool to define and optimize processing parameters and other factors influencing the temperature distribution for typical, industry-relevant geometries and materials. It is expected that modeling reduces significantly the number of experimental trials needed to define the processing parameters, and thus provide substantial time and cost savings.

Acknowledgement

References

[1] Fundamentals of Friction Welding, ASM Handbook, Welding, Brazing and Soldering, vol. 6, ASM International, 1994.
[2] D. Nicholas, E. Watts, Adv. Mater. Processes 139 (2) (1991) 47.
[3] A. Vairis, M. Frost, Wear 217 (1998) 117.
[4] V.I. Vill, Am. Weld. Soc. (1962).
[5] C.J. Cheng, Weld. J. Res. Suppl. 41 (12) (1962) 542-s.
[6] P. Kes, Beitrag zum Reibschweißen duktiler Eisengusswerkstoffe, DVS-Verlag, 1989.
[7] G. Wichelhaus, Schw. Schn. 27 (Heft 1) (1975) 9–10.
[8] O.T. Midling, Ø. Grong, Acta Metall. Mater. 42 (5) (1994) 1595.
[9] Ahmet Z. Sahin, Bekir S. Yibas, M. Ahmed, J. Nickel, J. Mater. Process. Technol. 82 (1998) 127.
[10] M. Kleiber, A. Sluzalec, Rozpr. Inz. 32 (1) (1984) 107.
[11] J. Ruge, K. Thomas, S.-joo Na, Abhandl. Braunschw. Wiss. Gesell., Band XXXV, Verlag Erich Goltze, Göttingen, 1983, pp. 89–109.
[12] K.K. Wang, P. Nagappan, Weld. Res. Suppl. 49 (H.9) (1970) S.419-s.
[13] L. Fu, L. Duan, Weld. Res. Suppl. (May) (1998) 202s.
[14] L. Wang, M. Preuss, P.J. Withers, G.J. Baxter, P. Wilson, J. Neutron Res. V12 (1–3) (2004) 21.
[15] H.W. Zhang, Z. Zhang, J.T. Chen, J. Mater. Process. Technol. 183 (2007) 62.
[16] Suck-joo Na, J. Ruge, K. Thomas, Schw. Schn. 36 (Heft 3) (1984) 121.
[17] H.-J. Krause, Metall. Construct. (June) (1983) 331.
[18] Thomas Hazlett, Weld. Res. Suppl. 10 (1962) 448-s.
[19] L. D'Alvise, E. Massoni, S.J. Walløe, J. Mater. Process. Technol. 125–126 (2002) 387.
[20] A. Sluzalec, Int. J. Mech. Sci. 32 (6) (1990) 467.
[21] A. Vairis, M. Frost, Mater. Sci. Eng. A292 (2000) 8.
[22] ANSYS Inc., Theory reference.
[23] V.E. Rubtsov, A.V. Kolubaev, J. Friction Wear 28 (1) (2007) 65.
[24] C.V. Madhusudana, Thermal Contact Conductance, Springer Verlag, New York, 1996.
[25] P. Wriggers, C. Miehe, Comput. Methods Appl. Mech. Eng. 113 (1994) 301.
[26] V.A. Karin, Teplovye osnovy svarki, Lehrbuch, LTTU, Leningrad, 1990 (in Russian).
[27] P. Wanjara, M. Jahazi, Metall. Mater. Trans. A 36A (8) (2005) 2149.
[28] M. Peters, C. Leyens, Titan und Titanlegierungen, Wiley-VCH, 2002.
[29] Base material characterisation, Microstructures and Mechanical Properties, Technical Report, Projekt "DUTIFRISK", 1.05.2004.
[30] O. Roder, Final Technical Report, Project "Dutifrisk", September 2006.
[31] R. Boyer, G. Welsch, E.W. Collings, Materials Properties Handbook: Titanium Alloys, ASM International, 1994.
[32] Ermittlung des Gleitreibwertes μ, Internal Report, MTU, 2006.
[33] A. Vairis, M. Frost, Mater. Sci. Eng. A271 (1999) 477.
[34] A. Vairis, N. Christakis, Int. J. Modell. Identification Control 2 (4) (2007) 347.
[35] R. Furlan, Thesis, Institut für Metallkunde und Werkstoffprüfung der Montanauniversität Leoben, 1996.
[36] F. Bethlehem Wilhelm, Schw. Schn. 36 (1984) 479. Heft 10.
[37] D. Sun, Zh. Ren, Zh. Zhou, J. Mater. Sci. Technol. 16 (1) (2000) 59.
[38] M.R. Daymond, N.W. Bonner, Physica B325 (2003) 130.
[39] W.-Y. Li, T.J. Ma, S.Q. Yang, Q.Z. Xu, et al., Mater. Lett. 62 (2) (2008) 293.
[40] M. Karadge, M. Preuss, C. Lovelli, et al., Mater. Sci. Eng. A459 (2007) 187.
[41] T. Mohandas, D. Banerjee, V.V. Kutumbarao, Mater. Sci. Eng. A289 (2000) 70.
[42] S.D. Meshram, T. Mohandas, G. Madhusudhan Reddy, J. Mater. Process. Technol. 184 (2007) 330.
[43] S. Anik, L. Dorn, G. Faninger, Schw. Schn. 32 (1980) 184. Heft 5.
[44] M. Majdic, G. Ziegler, Z. Metallkd. 65 (Heft 3) (1974) 173.
[45] R. Ding, Z.X. Guo, Mater. Sci. Eng. A 365 (2004) 172.